Sveriges lantbruksuniversitet
Swedish University of Agricultural Sciences

Department of Soil and Environment

UNIVERSITY OF COPENHAGEN

Imaging the 3D distribution of cation adsorption sites in undisturbed soil

Hannes Keck

Master's Thesis in Environmental Science
EnvEuro – European Master in Environmental Science

Examensarbeten, Institutionen för mark och miljö, SLU
2016:20

Uppsala 2016

Imaging the 3D distribution of cation adsorption sites in undisturbed soil

Hannes Keck

Supervisor: Johannes Koestel, Department of Soil and Environment, SLU
Assistant supervisors: Bjarne W. Strobel, Department of Plant and Environmental Sciences, University of Copenhagen & Jon-Petter Gustafsson, Department of Soil and Environment, SLU
Examiner: Nicholas Jarvis, Department of Soil and Environment, SLU

Credits: 30 ECTS
Level: Second cycle, A2E
Course title: Independent Project in Environmental Science - Master´s thesis
Course code: EX0431
Programme/Education: EnvEuro – European Master in Environmental Science 120 credits

Place of publication: Uppsala
Year of publication: 2016
Title of series: Examensarbeten, Institutionen för mark och miljö, SLU
Number of part of series: 2016:20
Online publication: http://stud.epsilon.slu.se

Keywords: cation exchange capacity, X-ray scanning, soil structure, contrast agent, heterogeneity

Sveriges lantbruksuniversitet
Swedish University of Agricultural Sciences

Faculty of Natural Resources and Agricultural Sciences
Department of Soil and Environment

Abstract

Most soil system models assume that the cation adsorption sites in soils are accessible and homogeneously distributed in space. This assumption is likely to be invalid, which may have significant consequences on the performance of these models. The cation exchange capacity (CEC) as a measure of the abundance of cation adsorption sites is commonly positively correlated with the soils' clay and organic matter content. Several studies have given evidence of spatially varying contents of soil organic matter and clay in the sheaths of biopores or as illuvial clay accumulation. This suggests that cation adsorption sites are not homogeneously distributed and not equally accessible. In order to investigate the 3D distribution of the cation adsorption sites in undisturbed soils, eight small soil cores (approx. 30 cm^3) were sampled from different locations. Their cation adsorption sites were saturated with Ba^{2+} in the laboratory. Ba^{2+} is widely used as index cation for standard procedures to measure the CEC and as a contrast agent in X-ray scanning. Before and after Ba^{2+} saturation the samples were scanned using an industrial X-ray scanner. 3D difference images of the soil cores were obtained by subtracting the first from the second image. These were interpreted as depicting the Ba^{2+} bound to cation adsorption sites only. The results show that the cation adsorption sites are heterogeneously distributed in space. One sample showed an increase in cation adsorption sites in biopore sheaths as compared to the soil matrix, others did not show a clear relation of the location of cation adsorption sites to pore structure. Our method correlates significantly with results of the commonly used ammonium acetate method to determine CEC and with a geochemical model describing the CEC for each sample. For the first time we were able to visualize the heterogeneous distribution of cation adsorption sites in undisturbed soil.

Key words: *cation exchange capacity, X-ray scanning, soil structure, contrast agent, heterogeneity*

Popular Summary

The amount of nutrient binding sites (cation adsorption sites) of a soil is one important factor to evaluate the soils' agricultural fertility and its function as a water filter. The interactions between nutrients or pollutants and their binding sites in soils are well understood but the effect of the spatial arrangement of these sites on plant growth and on the soils' filtering capacity is less well investigated. Recent studies suggest that these binding sites are not evenly distributed in space and may have an influence on nutrient and pollutant transport to ground water or on root growth of plants. Modern X-ray scanners can provide high quality, three-dimensional images of undisturbed soil cores, thus when the natural alignment of the soil aggregates is preserved. Similar to medical X-ray scanning, we can utilize contrast agents to study objects of interest within soil. Barium ions are often used as such contrast agents. The advantage of barium ions compared to other contrast agents is that they also bind on the nutrient binding sites in soils, which enabled us to image and study the arrangement of these in 3D. To our knowledge this was not yet done. Therefore, our aim was to obtain 3D images of the nutrient binding sites in soils and to validate our method with a standard laboratory procedure as well as a mathematical model that both determine the amount of nutrient binding sites only. Results show that the nutrient binding sites are unevenly distributed within the soil. One sample showed a higher abundance of cation adsorption sites around macropores compared to the soil interior, others did not show a clear relation to their pore structure. Our method correlates significantly with the standard laboratory procedure and with the mathematical model and we were able to visualize the heterogeneous distribution of nutrient binding sites in undisturbed soil for the first time.

Table of Contents

Index of Figures

Index of Tables

Introduction

Cation adsorption

Soil particle surfaces possess functional groups that are negatively charged. These interact electrostatically with cations and bind them reversibly (cation adsorption sites) (Essington, 2004). Typically a soils cation adsorption sites are positively correlated with its clay and organic matter (OM) content (e.g. Essington, 2004; Kahle et al., 2003, 2002). The amount of adsorption sites per mass of soil is referred to as the cation exchange capacity (CEC). It is commonly measured in cmol (+) kg^{-1} soil using Ba^{2+} or NH_4^+ to replace non-specifically retained cations in the outer sphere complexes or in the diffuse ion swarm of the solid-solution interface (Essington, 2004). The CEC determines agricultural soil fertility and the soils nutrient retention capacity (e.g. Cardoso et al., 2013; Murphy, 2015). Furthermore, it influences heavy metal retention (Darmawan and Wada, 1999; Gomes et al., 2001; Isoyama and Wada, 2007) and the mobility of cationic pesticides or other cationic pollutants in soils (Dollinger et al., 2015; Figueroa-Diva et al., 2010; Okada et al., 2016; Porfiri et al., 2015).

Heterogeneity of cation adsorption sites

The content and quality of clay or OM varies within soils depending on the bedrock, soil type, pedologic history, land use practices, vegetation cover, climate factors and biological activity (Guo and Gifford, 2002; Horn, 1987; Leue et al., 2010; Teferi et al., 2016). Biopores (e.g. earthworm borrows, root channels) often create preferential flow paths and hot-spots of biological activity with higher OM contents compared to the surrounding soil matrix, leading to a spatially heterogeneous distribution of OM as well as cation adsorption sites (Bundt et al., 2001a, 2001b; Jarvis, 2007; Kögel-Knabner et al., 2008). Peth et al. (2014) demonstrated visually the heterogeneous 3D distribution of OM in undisturbed soil using synchrotron X-ray microscopy. Illuvial clay

accumulation in argic horizons and the formation of clay cutans leads to a spatially heterogeneous distribution of clay (FAO, 2014). Also, Horn (1987) attributed a pronounced increase in fine material and CEC at aggregate surfaces to the aggregates shrinking and swelling activities, leading to separation of fine and coarse material. Thus, spatial variations of clay or OM content and type in the soil profile at the micro or macro-scale affects the spatial distribution of cation adsorption sites (Bundt et al., 2001b; Ellerbrock and Gerke, 2004; Horn, 1987). It may further determine the soils filtering properties, the location of plant nutrients, root growth and other biochemical processes.

Three dimensional imaging

3D imaging techniques bear great potentials to study and illustrate relationships and feedback mechanisms between structural and biochemical soil properties within undisturbed soil (e.g. Peth et al., 2014; Thieme et al., 2003; Tracy et al., 2010). Soil pore structure provides the spatial boundary for biologic activity within soils by compartmentalization and it determins the accessibility of water, air and nutrients (Ekschmitt et al., 2008; Ruamps et al., 2011; Young et al., 2008). This complex structure can be studied for its implications on biochemical processes using 3D imaging. A common method in X-ray computed tomography is to visualize the objects or processes of interest by enhancing their X-ray photon attenuation using contrast agents. Koestel and Larsbo (2014) used iodide in order to increase the X-ray photon attenuation of water to study water flow in an undisturbed soil column. Peth et al. (2014) imaged the OM distribution in soil using osmium as a contrast agent which is known to bind strongly to OM. A suitable contrast agent should contain element(s) with a higher atomic number than other common elements present in the soil. Furthermore, it must have an affinity to bind to or to dissolve in the object of interest (Van Loo et al., 2014). Such an agent increases the electron density and the X-ray photon attenuation locally by absorbing or scattering a proportion of the primary X-ray beam (Wildenschild et al., 2002). Ba^{2+} is a suitable contrast agent in X-ray computed tomography (Pauwels et al., 2013; Van Loo et al., 2014). It has a relatively high electron density (54), it binds to cation adsorption sites and it is

scarcely present in natural soils.

Aim

To our knowledge variations in the CEC in undisturbed soil cores were not yet imaged in 3D. Ba^{2+} as a contrast agent for X-ray scanning can be used to image the cation adsorption sites in 3D because it has a high affinity to replace other cations from adsorption sites and is used as a standard method to measure the cation adsorption. Therefore, the objectives of this project are (i) to visualize the cation adsorption sites of undisturbed soil samples in 3D using an industrial X-ray scanner and Ba^{2+} as a contrast agent, (iii) investigate the spatial distribution of cation adsorption sites with respect to the distance of soil macropores and (ii) to relate the CEC determined by 3D image analyses of the Ba^{2+} saturated soil sample with the CEC determined by traditional laboratory analysis using ammonium acetate and to geochemical model simulations.

Materials and Methods

Site description and sampling

Eight undisturbed, natural soil samples were taken with aluminum columns (height: 5 cm, diam: 2.2 cm) such that approximately half of the column volumes were filled with soil. The sample numbers (SNO) 1-4 were taken from a long term field trial, the Swedish fertility experiments (Kungsängen, R3-9001; Tab. 1) established in 1963 close to Uppsala. SNO1 and SNO3 at a depth of 3-5 cm and SNO2 and SNO4 at a depth of 35-38 cm corresponding to the plow pan. These samples have a high clay content and show earthworm activity (Fig. 1). SNO 5 - 7 originate from a soil located in a marshy depression which is periodically water logged. This soil is high in organic matter (OM) and classified as heavy clay (Tab. 1, 2 and Fig. 1). SNO 8 originates from a loamy sand and organic matter rich forest soil (Tab. 2 and Fig. 1). In addition, two artificial samples were included in the experiments (SNO 9 and 10) in order to visualize the difference in Ba^{2+} binding efficiency of clay and organic matter separately. They contained fine sand with several clay and peat aggregates.

Tab. 1: Total carbon (Tot. C), carbonate carbon (Carb. C) and organic carbon (Org. C) and location of each sampling site.

Site	Location	Tot. C [%]	Carb.C [%]	Org.C [%]
Kungsängen (3-5 cm)	59°50'10.9"N 17°41'15.2"E	2.18	0.02	2.17
Kungsängen (35-38 cm)	59°50'10.9"N 17°41'15.2"E	2.37	0.03	2.34
Periodically saturated soil	59°49'26.3"N 17°39'44.5"E	4.80	0.02	4.78
Forest soil	59°49'27.1"N 17°39'46.8"E	4.77	0.01	4.76

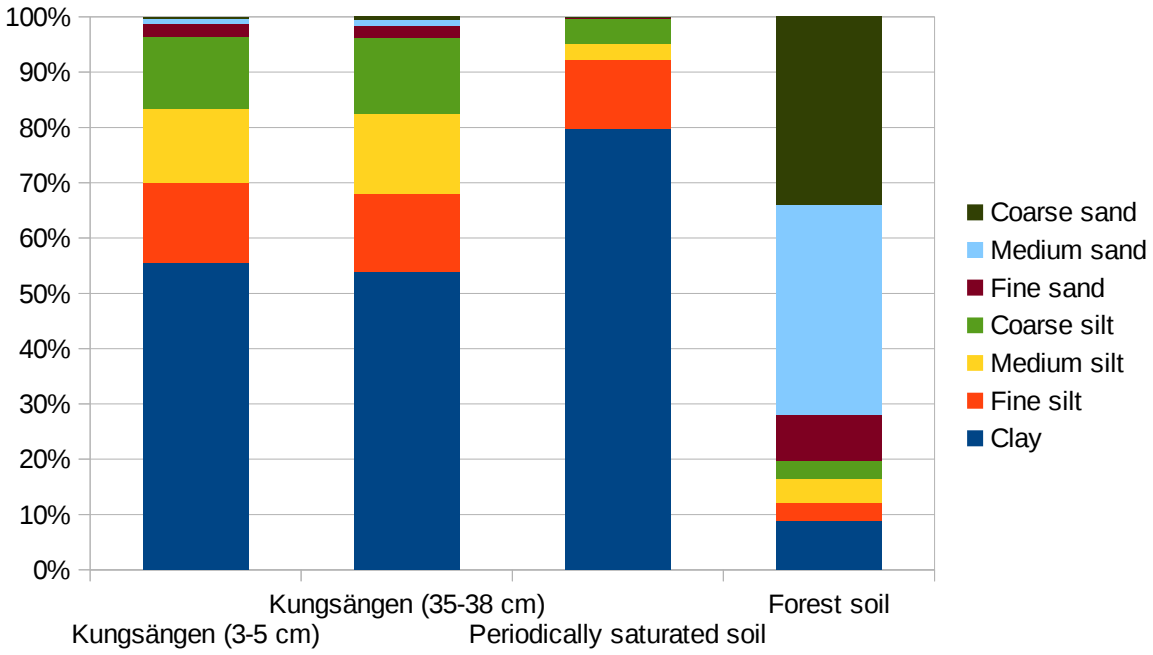

Fig. 1: Particle size distribution for each sampling area.

Tab. 2: Soil texture classes, sampling site, pH, cation exchange capacity (CEC_{NH4^+}) and bulk density (BD) for each sample number (SNO).

SNO	Soil texture	Site	PH [H_2O]	CEC [cmol kg^{-1}]	BD [g cm^{-3}]
1	Silty clay	Kungsängen (3-5 cm)	6.5	20.3	1.14
2	Silty clay	Kungsängen (35-38 cm)	6.5	19.1	1.30
3	Silty clay	Kungsängen (3-5 cm)	6.2	19.9	0.87
4	Silty clay	Kungsängen (35-38 cm)	6.3	20.4	1.20
5	Heavy clay	Periodically saturated soil	7.1	47.9	0.48
6	Heavy clay	Periodically saturated soil	6.8	22.0	0.41
7					0.56
8	Loamy sand	Forest soil	5.1	13.1	0.96
9 and 10	Fine sand	-	4.9	3.0	-
9 and 10	Clay aggregates	-	7.0	16.9	-
9 and 10	Peat aggregates	-	6.7	45.7	-

Laboratory analyses

In order to evaluate the precision of the $CEC_{Ba^{2+}}$ determined through the method described below the CEC_{NH4^+} was determined by the ammonium acetate method using NH_4^+ as index cation on sieved (< 2 mm) and air dried samples at pH 7. Tecator flow injection analysis (Foss A/S, Denmark) was used to measure the NH_4^+ contents. The soil pH was measured for all samples using the pH meter PHM 93, Radiometer Copenhagen, Denmark in deionized water. The particle size distribution was analyzed by sedimentation after removal of carbonates and organic matter by using hydrochloric acid (1 mol * L^{-1}) and hydrogen peroxide (30 %) respectively. The soil texture classes were determined according to FAO (2006). Total carbon contents were analyzed by the loss on ignition method for each sample location (TruMac CNS, LECO Corporation, MI, USA) and corrected by the carbonate content to give organic carbon. The bulk density was obtained after all analyses were completed and all samples dried at 105 °C by gravimetry. The soil mass was then related to the sample volume obtained by the 3D images. The bulk densities were corrected by the calculated Ba^{2+} mass adsorbed by each sample.

X-ray computed tomography imaging

The GE Phoenix *v|tome|x m* X-ray scanner installed at the Department of Soil and Environment at the Swedish University of Agricultural Sciences, Uppsala was used in this study. It is equipped with a 16 inch monitor (GE DRX250RT), a 240 kV X-ray tube with a tungsten target and a beryllium window. The samples where scanned at a maximum photon energy of 80 kV and an electron flow of 250 µA. The 3D images where obtained by combining 2000 radiographs taken over a time of 46 – 90 minutes, depending on the density of the sample, thus the exposure time per radiograph was 333 - 1000 µs. The radiographs were inverted using the GE software *datos|x* (version 2.1) and exported as 16 bit 3D *Tiff* images with a voxel size of 20 µm.

Experimental setup

The samples were placed on a sand bed and adjusted to a water tension of 100 cm for a period of three weeks (Tab. 3). Thereafter, the samples were placed onto fresh sand beds in plastic cups and saturated in a desiccator under a near-vacuum (Fig. 2) with a de-gased KCl solution (0.1 mol L^{-1}) to avoid air entrapment inside the columns. The samples were slowly saturated from the bottom up. Residual ions in the soil columns were washed out by daily removal of the supernatant and replenishment of the KCl solution outside the column (Fig. 3). Furthermore, the soil was given time for swelling. The electrical conductivity (EC) of the supernatant was measured at regular intervals (Device: Cond 3310, WTW GmbH, Weilheim, Germany) and the treatment stopped after the EC in the supernatant had reached the EC of the KCl solution with a tolerance of max. 2.5%. Each sample was scanned with the X-ray scanner in 3D resolution to obtain a reference images for later processing steps. No air entrapment was found in the reference images upon visual inspection.

All samples were then carefully transferred into new plastic cups filled with the 0.3 mol L^{-1} $BaCl_2$ solution. The samples were slowly saturated with $BaCl_2$ from the bottom up. In the following, the supernatant was daily removed and the $BaCl_2$ solution outside the column was replenished (Fig. 3). In this fashion the resident KCl solution was flushed out and cations on the cation adsorption sites were exchanged with Ba^{2+}. At regular intervals the EC of the supernatants was measured and X-ray images taken during the Ba^{2+} saturation process in order to find the time of Cl^- breakthrough and to monitor the spatial distribution of Ba^{2+} within the samples. The treatment was stopped after the EC in the supernatant of each sample had reached the EC of the $BaCl_2$ solution (max. tolerance of 2.5 %) and the gray values in the 3D X-ray images showed a temporally stable distribution. This was the case after 260 mL of $BaCl_2$ had been flushed through each sample.

In order to ensure that all non-adsorbed barium ions were washed out and potential $BaSO_4$ precipitates were redissolved, all samples were flushed by a 0.1 mol L^{-1} KCl solution over a period

of five weeks and 150 mL KCl solution per sample. After the EC of the supernatant had stabilized at the EC of the KCl solution (tolerance maximally 2.5 %), the KCl rinsing process was stopped and the final 3D images where taken of all samples. When the final images were taken the soil solution was equivalent to the KCl solution and the majority of the cation adsorption sites saturated with Ba^{2+}. In the following we refer to these images as 'Ba^{2+} saturated' images.

A 3D contrast image of the KCl and the $BaCl_2$ solution in separate plastic vials and the aluminum wall was obtained and used as a basis for the subsequent normalization process. Three samples (SNO4, SNO6 and SNO10) were excluded from further analyses. Two of them had been destroyed during the saturation process (SNO6 and SNO10) and one had a very small hydraulic conductivity and including it in the experiment would have exceeded the time available for this experiment.

Tab. 3: Experimental time schedule. X-ray scannings were performed after KCl treatment ($\boldsymbol{X_{REF}}$), after $BaCl_2$ saturation to check for a temporally stable distribution of gray values ($\boldsymbol{X}$) and after removal of residual Ba^{2+} ions ($\boldsymbol{X_{Ba}}$).

Tasks			
Adjustment to -100 mm			
Contrast image of $BaCl_2$, KCl and Al wall			
	KCl saturation		
	EC measurements	X_{REF}	
		$BaCl_2$ saturation	
		EC measurements	X
			Removal of residual Ba^{2+} X_{Ba}
Week 1 – 3	4 – 7	8 – 12	13 – 17

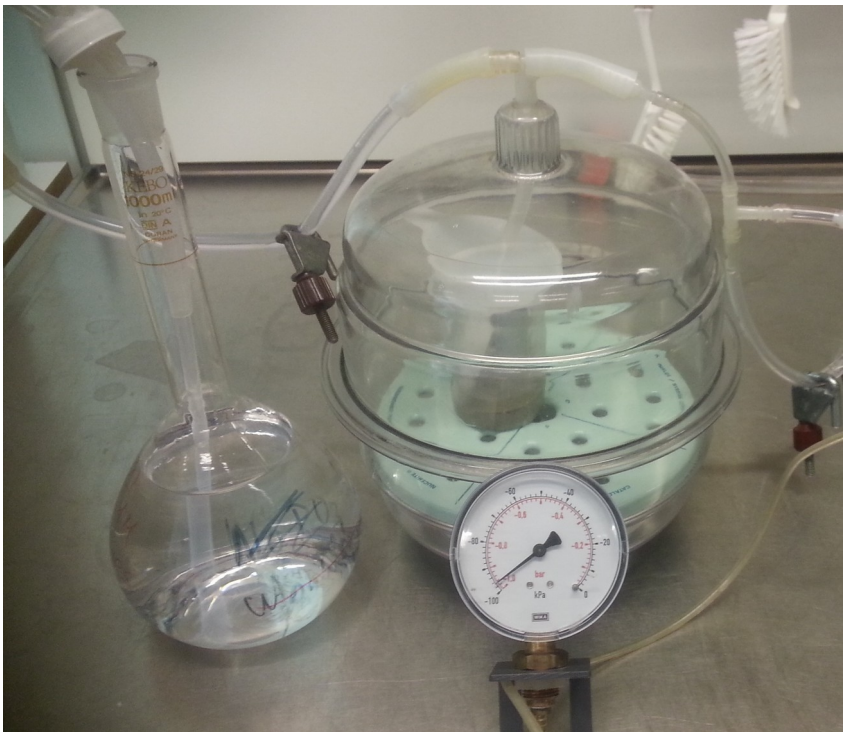

Fig. 2: Vacuum saturation setup.

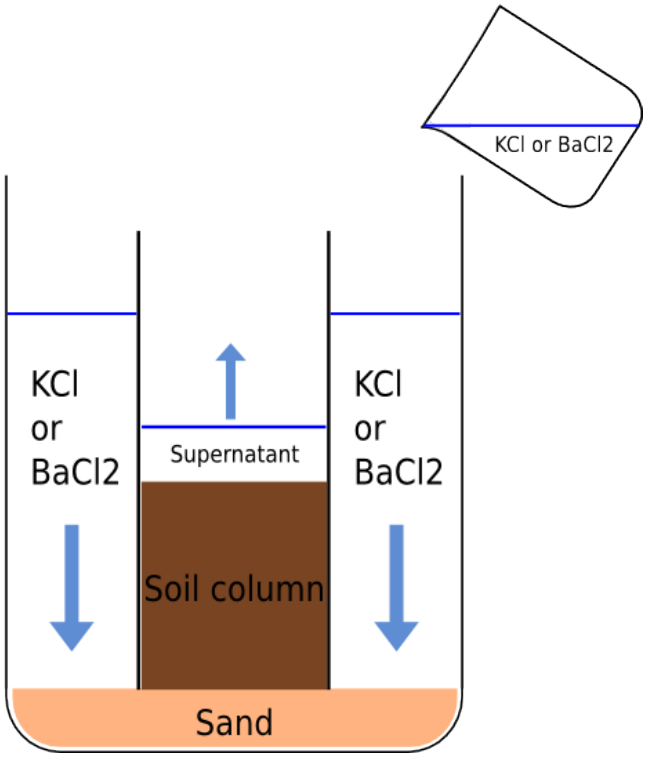

Fig. 3: Set up for the KCl or $BaCl_2$ saturation process.

Image Processing

The software ImageJ/FIJI was used for image processing (Schindelin et al., 2015, 2012). The resolution of all 3D images was reduced by a factor of 4 in order to reduce the image-processing time for the subsequent steps. Thus, the analyzed images had a resolution of 80 µm. The first step in the image processing was to straighten and center all images so that the column was upright and placed in the center of the canvas using the *ImageJ* plugin *SoilJ* with its function *StraigthenAndCenter* (Koestel, 2016). Furthermore, the illuminations of all images were corrected, so that all objects of the same density within individual images and across all images exhibited the same gray values (*SoilJ; FindColumnOutlines* and *NormalizeTheseImages*; Koestel, 2016). The mean gray values of the aluminum wall and the KCl solution in the contrast image (Fig. 4) were obtained and used as the target gray values for the normalization (21,418 and 16,225 respectively). All other gray values were scaled accordingly by the linear relationship between the target gray values and the initial gray values of the corresponding image. A 3D unsharp mask with one pixel radius was applied to all images in order to increase sharpness (*SoilJ*; *MedianFilterAndUnsharpMask3D*; Koestel, 2016). Both, the reference image and the Ba^{2+} saturated image were binarized using a threshold gray value of 16,976, which was obtained from the joint histogram of all images that were to be binarized (Fig 5; by *SoilJs'* function *HistoGrammar;* Koestel, 2016). This was done to obtain the pore space for both the reference image and the corresponding Ba^{2+} saturated image. The images were binarized using *SoilJs'* function *SegementThis (Koestel, 2016).*

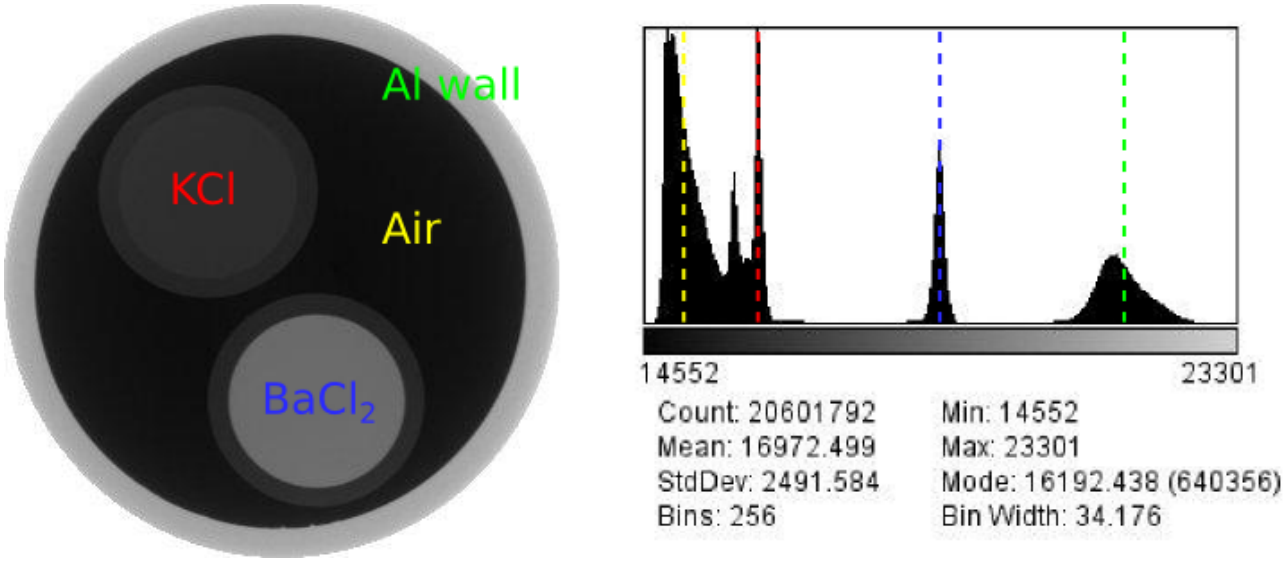

Fig. 4: Contrast image of the aluminum cylinder wall, KCl and $BaCl_2$ solution and the air (left). The corresponding histogram on the right with the mean values for the aluminum cylinder wall (green), KCl (red) and $BaCl_2$ (blue) solution and the air (yellow) indicated as dotted lines.

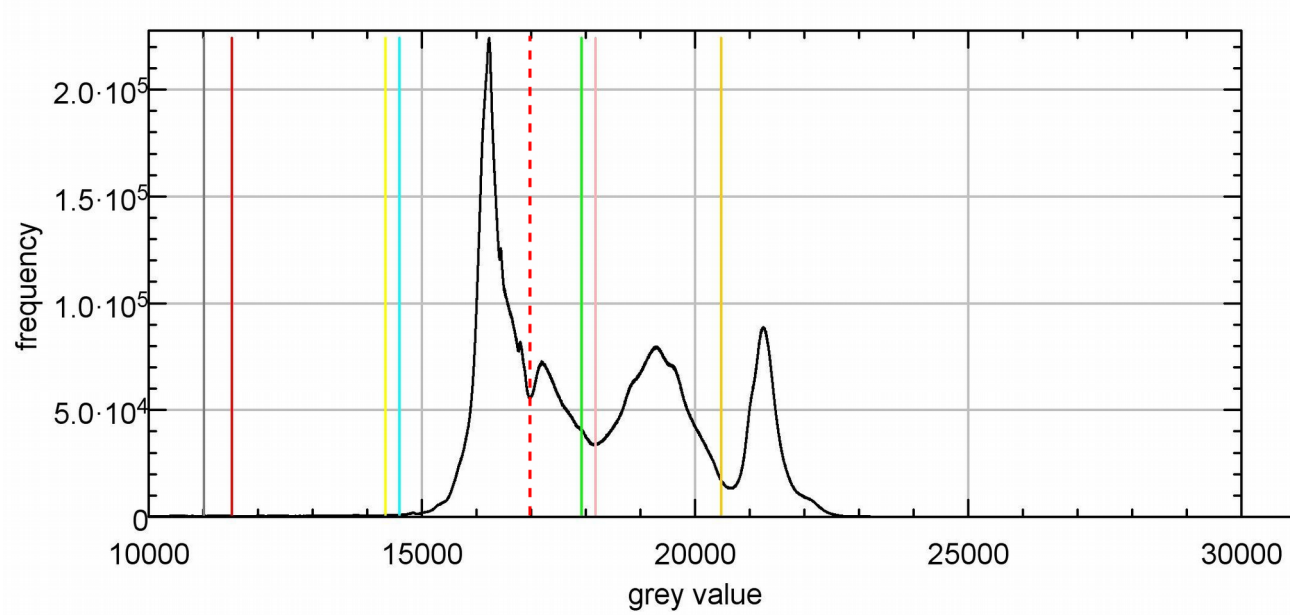

Fig. 5: The joint histogram of all images that were binarized. The red dotted line represent the segmentation threshold that was used for binarization, the other colored lines represent suggested segmentation thresholds according to a variety of methods.

Creating the difference images

The images were aligned in a way that all the objects of the Ba^{2+} saturated image were in the same

location as the corresponding objects in the reference image. In order to achieve this the images where registered using the *ImageJ* plugin '*descriptor-based series registration (2d/3d)*' by Preibisch et al. (2010) with the transformation model *affine* to account for minor soil deformations during the sample treatment. Thereafter, the difference images were obtained by subtracting the 3D Ba^{2+} saturated images (after the residual Ba^{2+} was flushed out) from the reference 3D images (before the $BaCl_2$ saturation started, when the samples were saturated with KCl solution). This was done by applying the *ImageJ* in-build *Image Calculator*.

Relationship between gray values and barium mass

In order to estimate the Ba^{2+} mass in the difference images as a proxy for the $CEC_{Ba^{2+}}$ the 3D contrast image of $BaCl_2$, KCl solutions and the aluminum wall was used as a reference (Fig. 4). The mean gray values of the two solutions were subtracted in order to obtain the maximal contrast in gray values (γ_{SAT} = 2637) corresponding to the density contrast between the KCl and $BaCl_2$ solutions. The $BaCl_2$ mass ($m_{j,d}$ in mg) was then calculated according to Koestel and Larsbo (2014) using the following equation:

$$m_{j,d} = \frac{V_{VOX} C_{MAX}}{\gamma_{SAT}} \gamma_{j,d}$$

where *j* is the voxel, V_{VOX} represents the voxels' volume (= $5.12*10^{-7}$ cm^3), C_{MAX} the maximal possible increase in tracer solution (= 41.199 mg * cm^{-3}) and γ the corresponding gray value. In order to calculate an estimate of the $CEC_{Ba^{2+}}$ in cmol (+) per kg soil the sum of the positive charged sites as occupied by Ba^{2+} was calculated and related to the samples volume and bulk density.

Spatial distribution of cation adsorption sites

In order to test whether the imaged CECs are elevated in macropore sheaths (400 µm distance from pore surface) as compared to the CECs in the soil matrix, the binarized 3D images of the pore space

for the reference and the Ba^{2+} saturated images were combined using the *Image Calculator*. This was done to account for any changes in pore space due to disturbances during the saturation periods. The resulting images of the combined pore space was dilated five times using the ImageJ plugin *Process* and its function *dilate 3D*. Subsequently, this dilated binary image was subtracted from the corresponding difference image in a way that the resulting image showed the gray values from the difference image only outside the pore space and the dilation area (only the soil matrix). After inverting the dilated binary image it was subtracted from the difference image and resulting in a second image that represents only the gray values in the dilation area, thus the soil around the macropores. These images were used to assess the difference of the imaged CECs between the soil close to macropores and the soil in the matrix of all natural soil samples.

Geochemical modeling

The Ba^{2+} that was bound to adsorption sites and in OM complexes at equilibrium in each sample was modeled using Visual MINTEQ (v3.1) (Gustafsson, 2012). As input data the soils pH and the concentrations of Ba^{2+} and Cl^{-} in the solution were used. Soil organic matter (SOM) was modeled with the Stockholm Humic Model (Gustafsson, 2001) by assuming SOM ≈ 1.72 × org.C and that SOM consists of 50 % fulvic and 50 % humic acids (Essington, 2004). The number of clay adsorption sites were approximated by the CEC measured in the laboratory by the ammonium acetate method. Furthermore, the clay adsorption sides were assumed to be saturated by K^{+}. In all simulations the temperature was set to 21 °C. The amount of Ba^{2+} that was adsorbed to adsorption sites and bound in OM complexes of each sample was then used to calculate the CEC (cmol (+) kg^{-1}) by relating it to the samples volume and bulk density and by multiplying it by two.

Statistical analyses and visualization

For statistical analyses the open source software *R* (v0.98.1x) and *RStudio* (v3.2.5) was used (R Core Team, 2016). The relation between measured CEC_{NH4^+} and the $CEC_{Ba^{2+}}$ obtained through image

analyses was analyzed by a linear model. The $CEC_{Ba^{2+}}$ distribution around the macropores of the natural soil cores were graphically compared. The graphical presentations of the X-ray images were prepared using *ImageJ/Fiji* (Schindelin et al., 2015, 2012) and *Inkscape* (v0.48). The statistical visualizations were done by using the *R* packages *ggplot2* (Hadley Wickham, 2009).

Results and Discussion

The Cl^- breakthrough curves in Fig. 6 show a uniform solute breakthrough of the seven intact samples. After removal of approximately 150 mL cumulative supernatant all samples reached a EC close to the EC of the $BaCl_2$ solution. A temporally stable distribution of $BaCl_2$ throughout all soil columns was observed by visual inspection of the 3D images after removal of 260 mL cumulative supernatant and 21.67 times (average; standard deviation = 4.66) the respective soil columns volume.

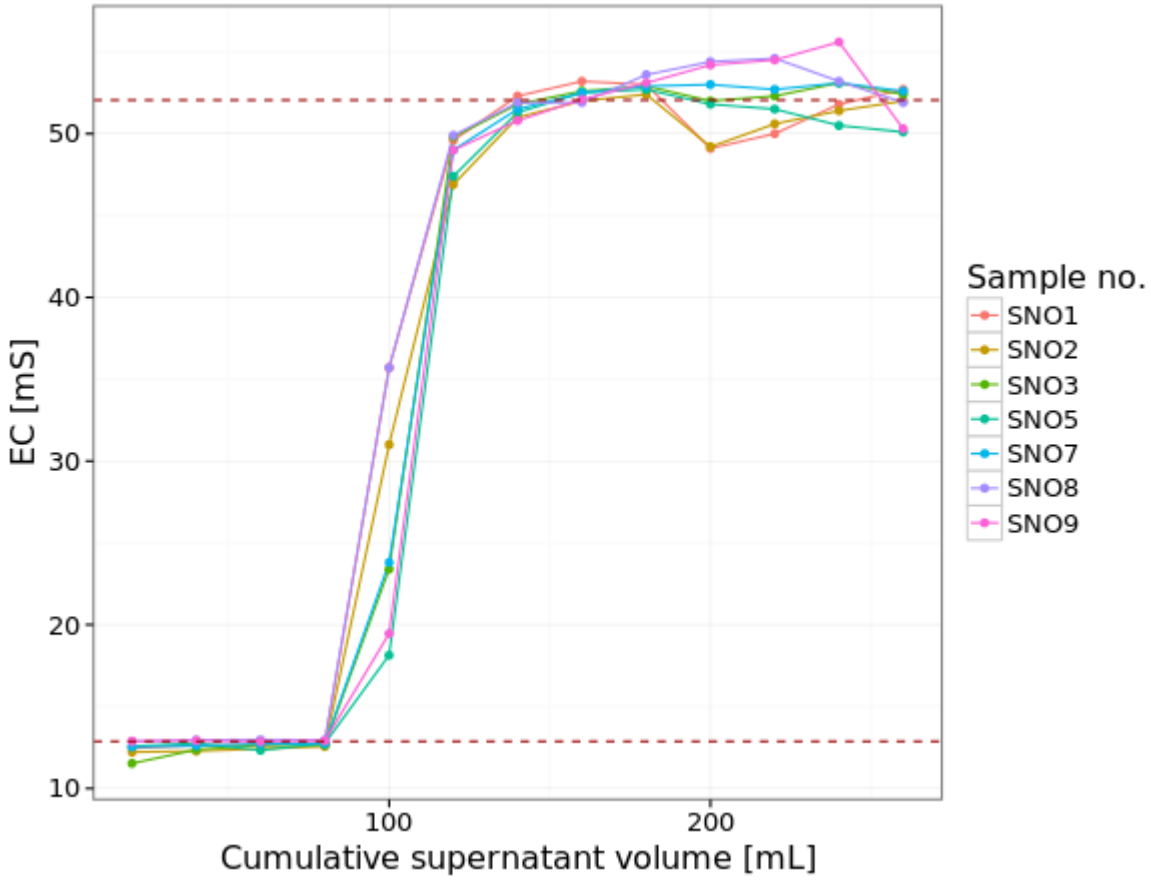

Fig. 6: Cl^- breakthrough curve based on the electric conductivity (EC) measurements over a period of 32 days for all seven samples. The dotted lines indicate the EC of the KCl solution (bottom) and the EC of the $BaCl_2$ solution (top).

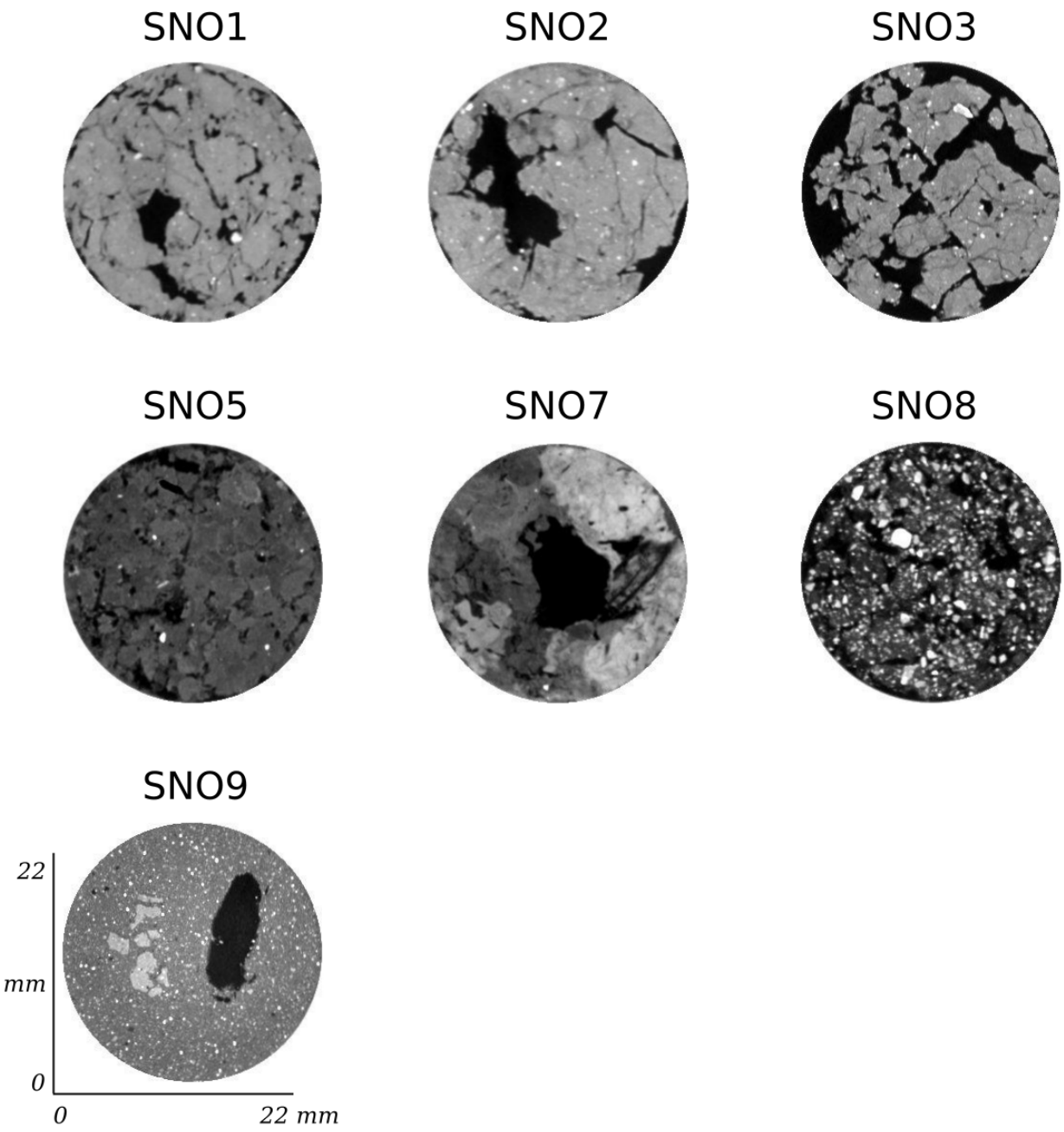

Fig. 7: Cross sections of the reference images of the seven intact soil samples. Depth from the soil surface: SNO1, 2 and 3 at 8 mm, SNO7 and 8 at 9 mm, SNO5 at 15 mm and SNO9 at 5 mm.

Fig. 7 shows cross sections of the reference images for the seven intact soil samples. The cross sections of the difference images in Fig. 8 correspond to those in Fig. 7 and show a varying degree of

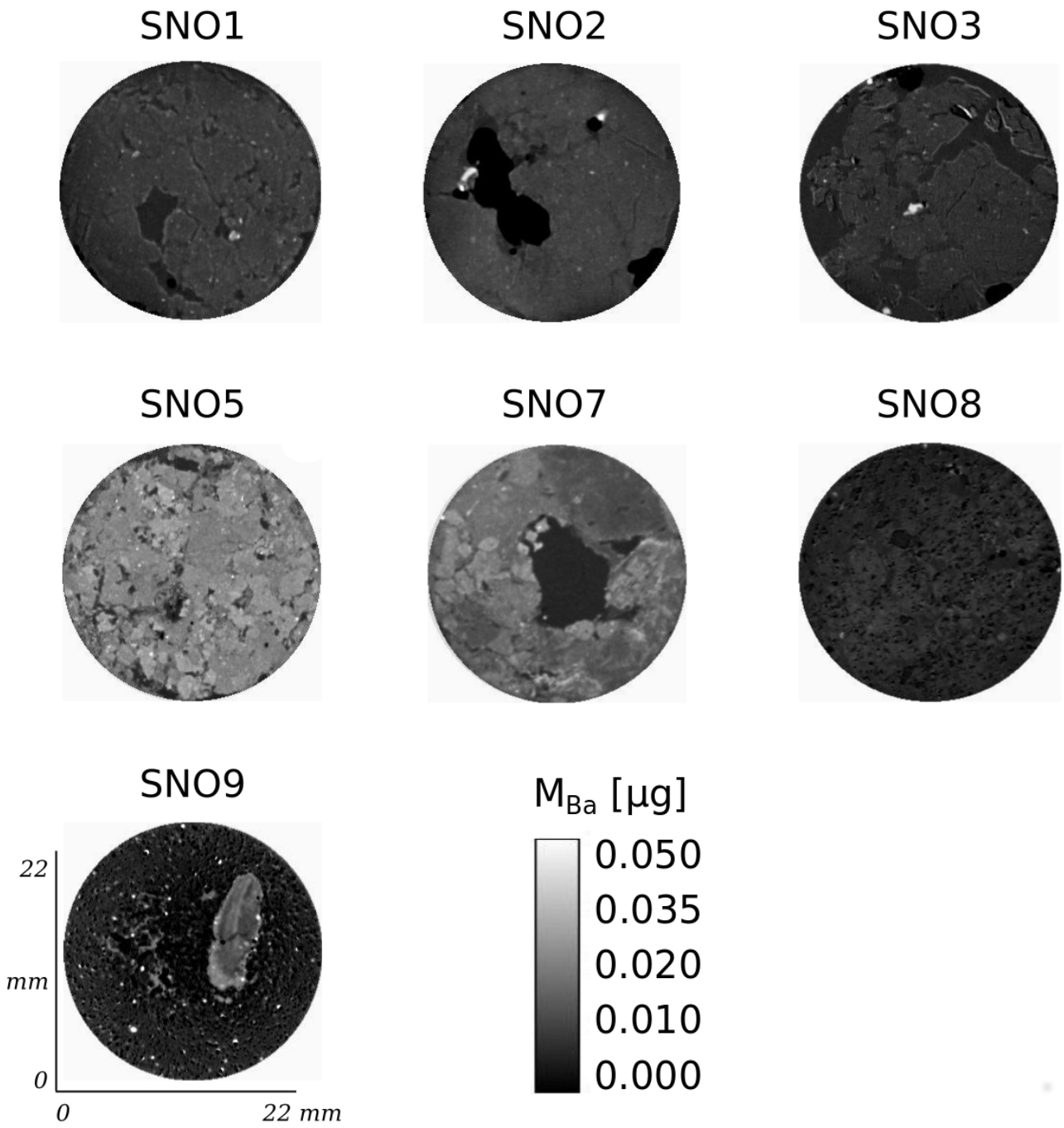

Fig. 8: Difference images of the seven intact soil samples. The gray scale indicated the Ba^{2+} mass (M_{Ba}) in µg. Depth from the soil surface: SNO1, 2 and 3 at 8 mm, SNO7 and 8 at 9 mm, SNO5 at 15 mm and SNO9 at 5 mm.

heterogeneity in the Ba^{2+} mass distribution. It is of no difficulty to differentiate between pores and soil matrix. Thus, most of the soils matrix possess cation adsorption sites abundant enough to be visualized by this method. The adsorbed Ba^{2+} mass (M_{Ba}) and its heterogeneity are particularly high in the heavy clay soils SNO5 and SNO7 (Fig. 8). Whereas, the other four undisturbed samples

(SNO1 to SNO3 and SNO8) have lower contrasts with a lower adsorbed Ba^{2+} mass. This pronounced difference between the samples reflects the variation in CEC_{NH4^+} and OM contents between them (Tab. 1 and 2). The artificial sample (SNO9) shows the highest gray values for OM, which is easy to differentiate from the sand and clay. Interestingly, the difference in gray values of the clay particles and the surrounding sand is much less distinct. The samples SNO1 and SNO3 show brighter gray values around macropores. A magnification of these brighter areas in Fig. 9 shows that in SNO1 they surround the entire pore walls (with an approximate thickness of 0.4 mm),which is likely due to accumulation of organic matter in

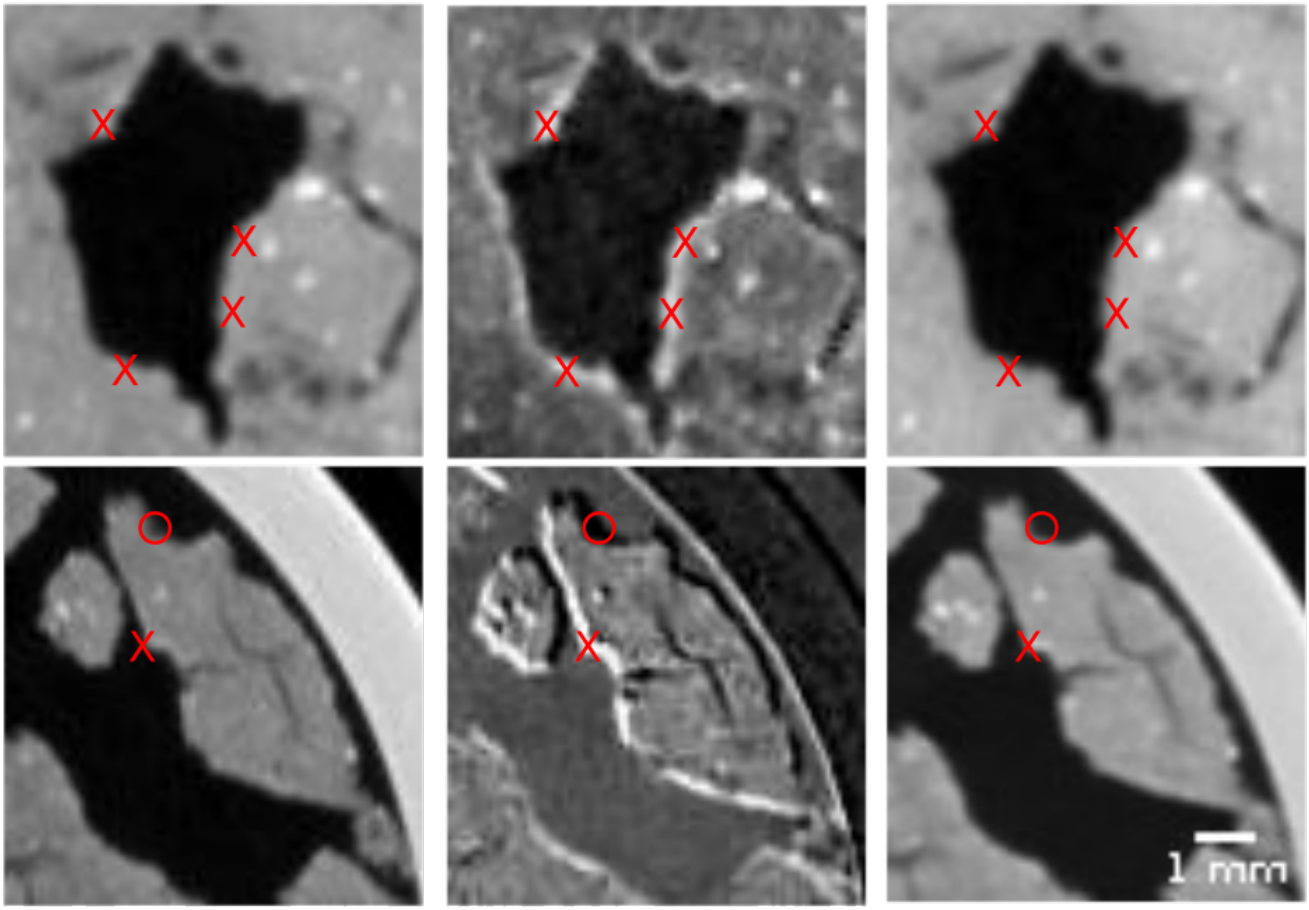

Fig. 9: Magnification of SNO1 (top) and SNO3 (bottom). Reference image (left), difference image (middle), Ba^{2+} saturated image (right). The red marks indicate the same positions in the three images.

earthworm burrows or other biopores and thereby a locally higher $CEC_{Ba^{2+}}$. Another explanation could be that the soil was swelling during the $BaCl_2$ saturation process, resulting in structural differences between the reference image and the Ba^{2+} saturated image. This hypothesis was checked

visually by comparing the location of the pore walls between the two images. No signs of swelling were observed, neither in horizontal nor vertical direction, thus this hypothesis was rejected (Fig. 9). In the difference image of SNO3 the brighter gray values are predominantly located on one side of the soil aggregates where the other side shows darker values. This is a typical sign for soil movement and can be explained by a shift of the aggregate after the reference image was taken. In the difference image this shift results in bright areas, if high gray values in the Ba^{2+} saturated image (e.g. soil matrix) are subtracted from low gray values in the reference image (e.g. soil pore) and in dark areas, if the reverse is the case. The very bright spot in the difference image of SNO2 in Fig. 8 is also due to such a shift. Fig. 10 demonstrates this visually. SNO8, the sandy sample, high in OM shows relatively little heterogeneity compared to the others (Fig. 8). But it is obvious that the coarse sand grains that are present in the sample have little cation adsorption sites binding Ba^{2+} and most of the adsorbed Ba^{2+} is present in the OM and fine material surrounding the sand grains (Fig. 11).

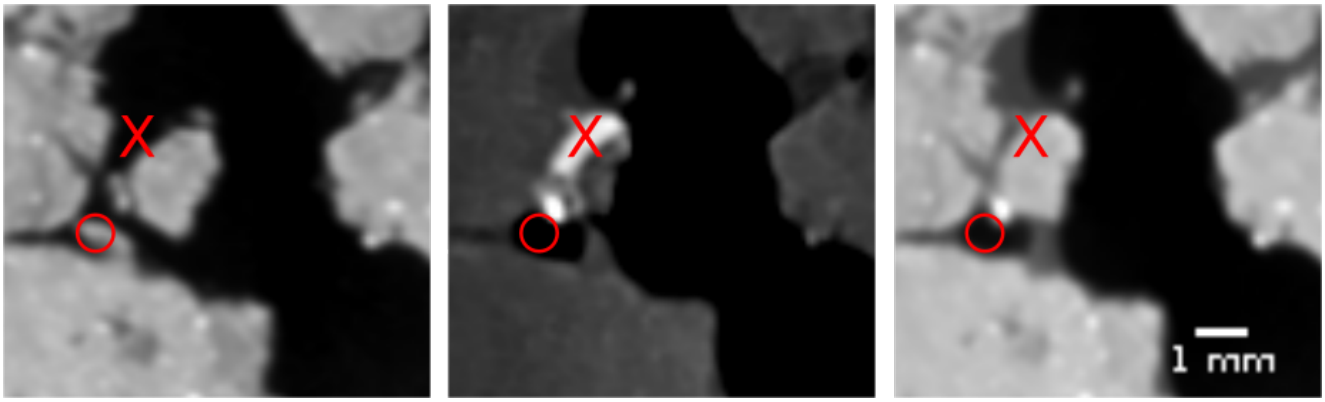

Fig. 10: Effect of aggregates movement on the difference image on the example of SNO2. Reference image (left), difference image (middle), Ba^{2+} saturated image (right). The red cross and circle indicate the same positions in all three images. It is easy to see that the movement of one soil aggregate resulted in very high gray values in the difference image.

Diagonal transects across the cross sections in Fig. 8 were analyzed for their gray values and corresponding Ba^{2+} mass distribution. Fig. 12 shows the Ba^{2+} mass distribution across these transects. This figure supports the observations made in Fig. 8. SNO5 and SNO7 show the highest Ba^{2+} mass with strong spatial heterogeneity. SNO3 and SNO8 show the least heterogeneity. The

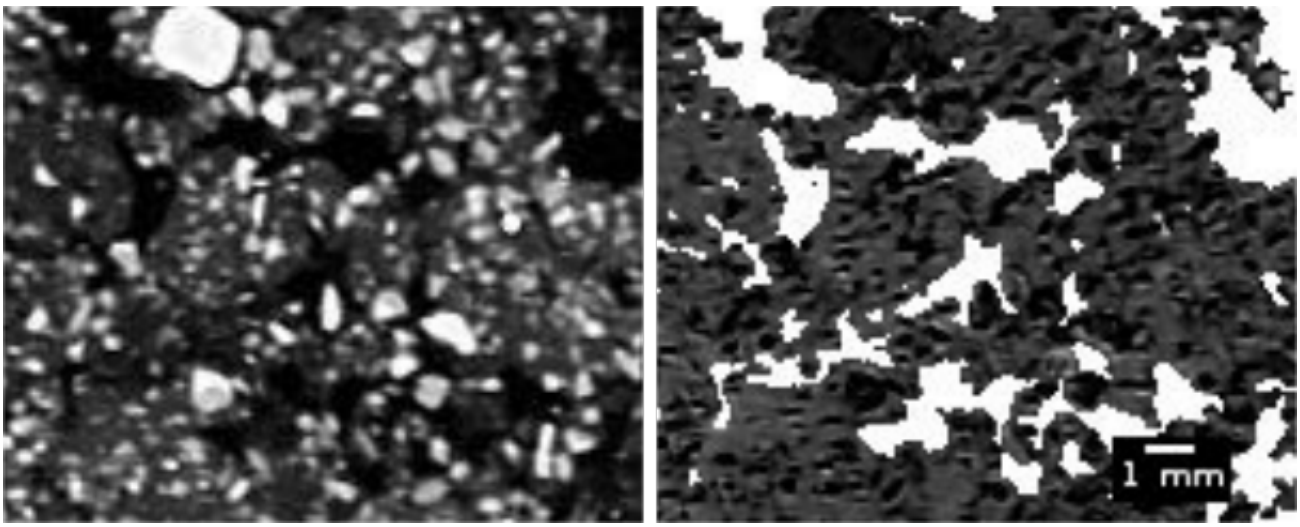

Fig. 11: Reference image (left) and difference image (right) including pore space in white of SNO8.

negative values for SNO2 at 2.5 mm distance correspond to the shifted soil aggregate marked with a red circle in Fig. 10. The negative values thereafter (4.5 to 8 mm distance) correspond with very low gray values due to air bubble formation during sample treatment. Similarly, SNO9 shows some evidence of sand gain movements, SNO8 of small air bubble formation and SNO3 of soil aggregate movements. These processes were found to be responsible for the gray values below zero in Fig. 12. The gray value distribution of the matrix space and the space in the macropore sheaths of the 3D difference images are presented in Fig. 13. For SNO1, and SNO7 the means (depicted as ◊ in Fig. 13) of the gray values within the matrix are clearly lower than those within the sheaths. For SNO3 and SNO8 there was no difference observed. For SNO2 and SNO5 the mean values within the matrix are higher. Like visually observed in Fig. 9 this comparison confirms the observation of higher gray values around macropores of SNO1.

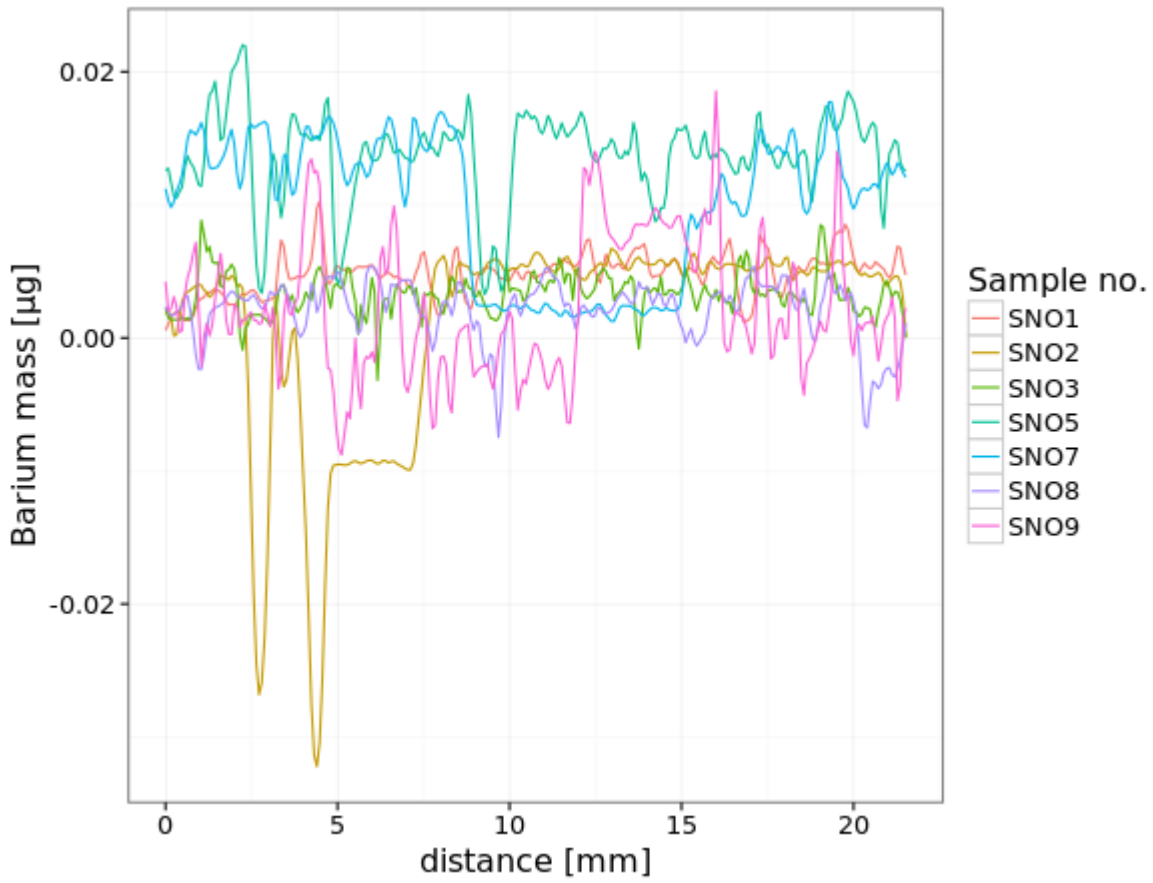

Fig. 12: Horizontal Ba^{2+} mass profiles of the seven soil samples.

The opposite is the case for SNO2, despite that the sample originates from the same location, only deeper down in the soil profile. The lower mean values for the macropore sheaths of SNO2 represent a lower abundance of cation adsorption sites within the macropore sheaths. This sample was taken from the plow pan and has the highest bulk density from all analyzed samples (Tab. 2). Thus, the lower gray values of the macropore sheaths may originate from lower OM contents within the sheaths compared to SNO1 possibly due to limited faunal activity (e.g. earthworm) within the plow pan (Capowiez et al., 2009). Also, air bubble formation during the experimental procedure was observed for SNO2 in particular, which may have blocked and limited the accessibility of the macropore sheaths as well as the exchange of K^+ by Ba^{2+}. SNO5 and SNO7 show very high heterogeneities in their gray value distribution, which seems not to be spatially related with the location of pores (Fig. 8). This is reflected in the high variation of gray values for the macropore sheaths and the soil matrix in Fig. 13. In SNO8 the sand grains are surrounded with OM and fine

material (see Fig. 11), thus they tend to be located further away from pore surfaces. Sand grains possess very few cation adsorption sites therefore, they are visible as darker spots in the difference image. This may be the reason for the lower mean gray value in the soil matrix of SNO8.

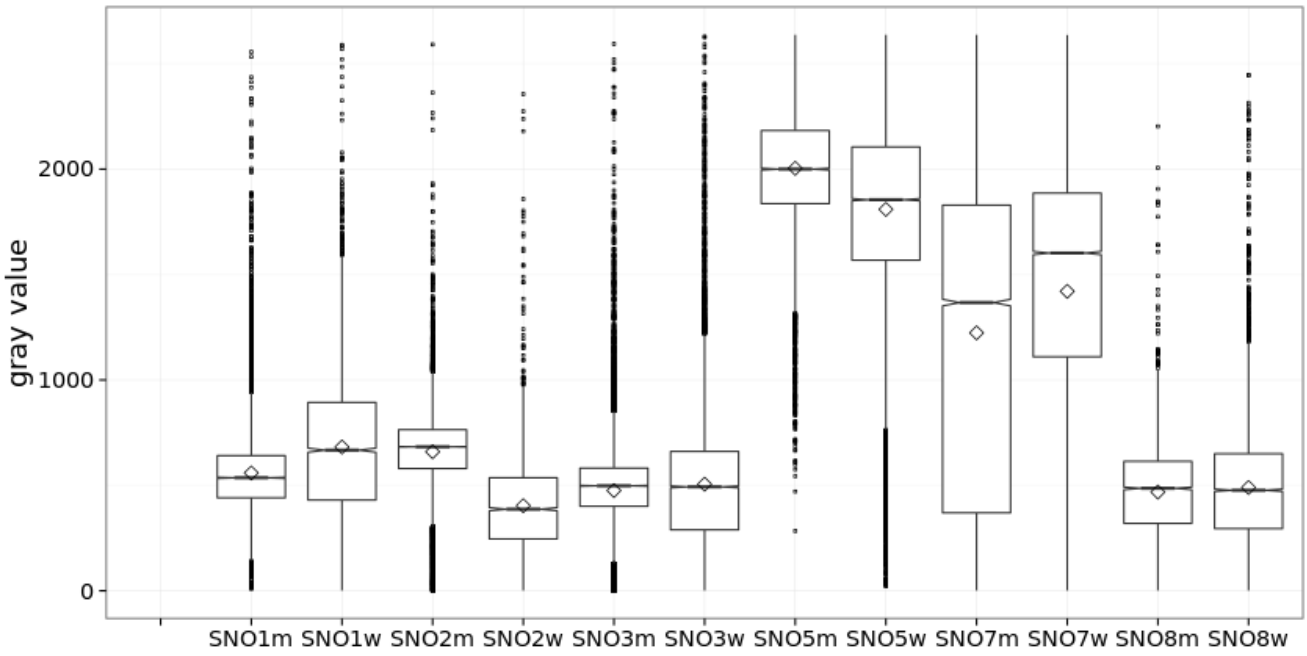

Fig. 13: Comparison of the gray value distributions close to the wall (w) and within the matrix (m) of the natural soil samples. The rhombus (◊) represents the corresponding mean values.

The correlation of the CEC_{NH4^+} measured in the laboratory with the $CEC_{Ba^{2+}}$ obtained from the difference images shows a significant relationship ($r^2 = 0.77$; $p < 0.05$; Fig. 14). Also, the correlation between the modeled CEC and the $CEC_{Ba^{2+}}$ is highly significant ($r^2 = 0.95$; $p < 0.001$, Fig. 15). Both confirm that the applied method is suitable to describe the CEC of the respective soil samples and strengthening the validity of our difference image results. The $CEC_{Ba^{2+}}$ values are lower by approximately two orders of magnitude compared to the CEC_{NH4^+} values and approximately one order of a magnitude lower than the modeled CEC values. This discrepancy between the methods can result from different factors. The laboratory analysis of CEC_{NH4^+} as well as the Visual MINTEQ are based on experiments on sieved, finely grinded soils, whereas our results of $CEC_{Ba^{2+}}$ are based on undisturbed soils. Some soil surfaces in pores not accessible to the $BaCl_2$ solution in the

undisturbed samples may not have been saturated with Ba^{2+} and did not contribute to then $CEC_{Ba^{2+}}$. When investigated as sieved soils these surfaces get exposed and more easily accessible, thus partisipating in ion exchange. Also, the extensive rinsing with the KCl solution (150 mL per sample) may have led to desorption of Ba^{2+} from cation adsorption sites and underestimated the $CEC_{Ba^{2+}}$. Depending on the difference in electron density between the replaced cations that initially were adsorbed to the adsorption sites and the Ba^{2+} that replaced them, the $CEC_{Ba^{2+}}$ will be underestimated to a different extent.

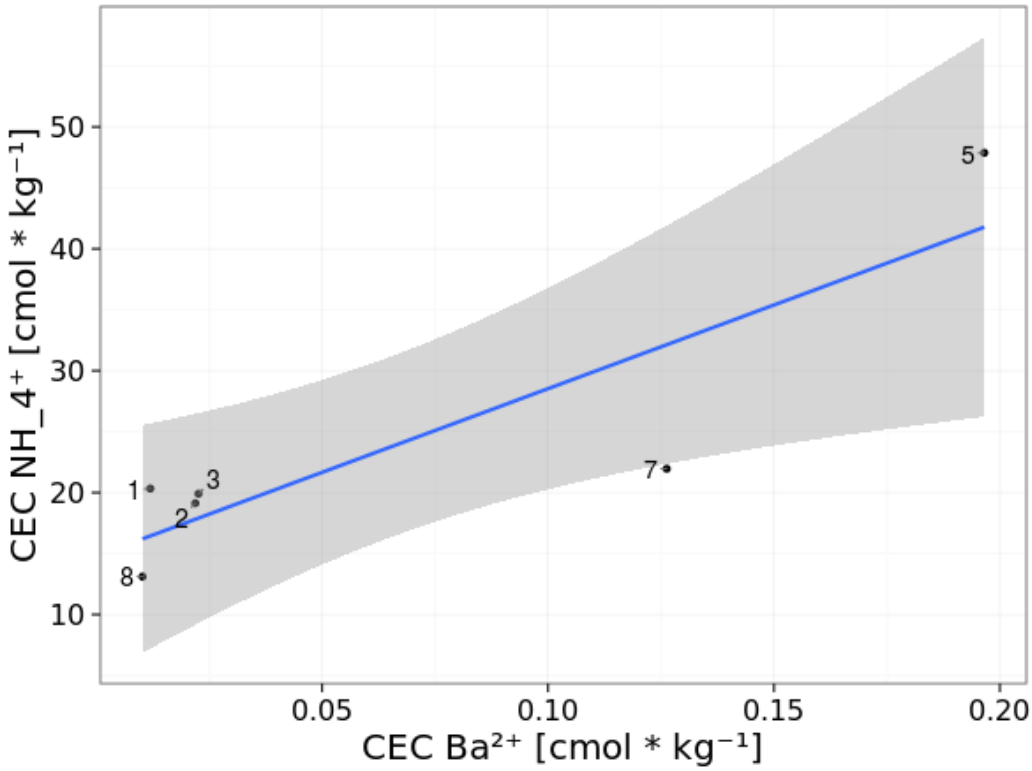

Fig. 14: Relation between the CEC measured with NH_4^+ and the CEC Ba^{2+} obtained from the difference image analysis of the natural soil samples, blue line represents a linear model with its 95 % confidence interval in gray ($p < 0.05$; r^2 0.77).

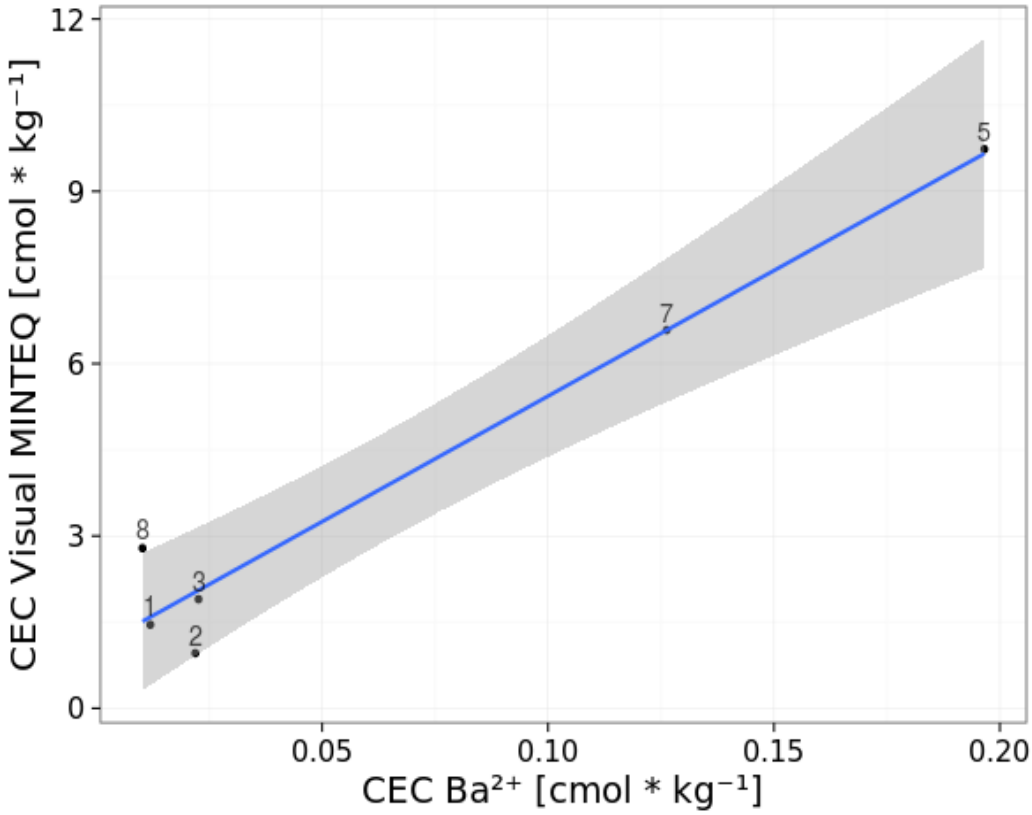

Fig. 15: Relation between the CEC modeled with Visual MINTEQ and the CEC Ba^{2+} obtained from the difference image analysis of the natural soil samples, blue line represents a linear model with its 95 % confidence interval in gray ($p < 0.001$; r^2 0.95)

Assuming that most adsorption sites were occupied by K^+ (18 electrons) when the reference images were taken and with Ba^{2+} (52 electrons) when the Ba^{2+} saturated images were taken the image contrast will be reduced by 33 %. If heavier elements were replaced by Ba^{2+} the contrast will be reduced even more. Also, we could not account for differences in the relation between image gray values and object densities between the reference image and the Ba^{2+} saturated image. We assumed the same linear relationship for both the reference image and the Ba^{2+} saturated image to be true. In case the relationship is non-linear and the introduction of a denser material (here Ba^{2+}) changes this relationship, the resulting difference images may not represent the Ba^{2+} densities only. This may be the case especially when extrapolating e.g. at densities larger than the aluminum wall. Using the two different index cations (Ba^{2+} and NH_4^+) to estimate the CEC can lead to different results (Ciesielski and Sterckeman, 1997; Jaremko and Kalembasa, 2014). In the presence of 2:1 clays like

smectites NH_4^+ may be trapped in the interfoliaceous cavities (Essington, 2004; Pansu and Gautheyrou, 2006). The ammonium acetate method may overestimate the CEC_{NH4^+} due to dissolution of $CaCO_3$ or $CaSO_4$. Furthermore, competition and displacement of Ba^{2+} on clay surface adsorption sites by K^+ can be rather strong due to their similar ionic radii (Kabata-Pendias, 2010). Therefore, the KCl rinsing process may have led to a reduction of local Ba^{2+} densities as well as the X-ray photon attenuation on clay surfaces and an underestimation in $CEC_{Ba^{2+}}$ of clay-rich samples. Ba^{2+} can be bound on OM in complexes (Bodek, 1988; Bradl, 2004; Lee et al., 2007; Pichtel et al., 2000) and competition with K^+ is less relevant, whereas, the single positive charged NH_4^+ is not prone to form complexes. Thus, the $CEC_{Ba^{2+}}$ may describe the CEC of OM better than the CEC of clay surfaces. It is also important to consider the actual soil pH especially when comparing a unbuffered ($BaCl_2$) with a buffered method (ammonium acetate) (Ciesielski and Sterckeman, 1997). However, all soil samples except SNO8 have pH values close to neutral (Tab. 2), thus the buffering of the ammonium acetate method at pH 7 will have little influence on the determined CEC_{NH4^+}. The most acidic soil sample was SNO8 (Tab. 2), here the CEC_{NH4^+} may be overestimated. The results of the Visual MINTEQ simulations described the $CEC_{Ba^{2+}}$ better than the CEC_{NH4^+} with a higher r^2 and p-value. The reason may be that the simulations included the formation of OM-Ba^{2+}-complexes. The deviation between the simulated CEC and the CEC_{NH4^+} may be due to the fact that we did not have data available on the clay mineralogy or the type of OM. Furthermore, the CEC_{NH4^+} was used as a proxy for the cation adsorption sites on clay minerals, but CEC_{NH4^+} includes also the CEC due to OM. This may have led to overestimation of the CEC in OM rich samples.

A heterogeneous distribution of cation adsorption sites in natural soils was described in several studies. Bundt et al. (2001a, 2001b) relates a higher abundance of adsorption sites to higher OM concentrations in preferential flow paths of a forest soil compared to its matrix. Altman et al. (2005) mapped caesium adsorption in soil aggregates and found them to be spatially related to the presence of iron enriched intergranular material. And Ellerbrock and Gerke (2004) found aggregate interiors

to possess a higher CEC compared to their OM enriched coatings, arguing that the clay rather then the OM dominated the CEC. In our study we found a high spatial heterogeneity in the distribution of cation adsorption sites for most analyzed soil samples. A heterogeneous distribution of adsorption sites in natural soil may have implications on the performance of soil system models. However, Masum et al. (2016) found that heterogeneity at millimeter scale has little influence on solute diffusion at centimeter scale, thus the assumption of homogeneity made by most soil system models may be justified. And Johnson et al. (2003) found spatially heterogeneous distribution of adsorption sites to be of secondary relevance when modeling contaminant transport. But the effect of a higher or lower CEC, especially within the macropore sheaths compared to the soil matrix, is little investigated and is still debated in literature (Jarvis, 2007). Considering a scenario in which solute transport bypasses 90% of the bulk soil volume, as shown by Koestel and Larsbo (2014), the location of adsorption sites may matter in order to improve the performance of soil system models, especially when modeling short distance solute transport. Only a few soil system models can take these differences into account (e.g. Larsbo et al., 2005).

Further Research

To further assess the relevance of spatially heterogeneous distributed adsorption sites for solute transport, it may be of interest to focus on active preferential flow paths in a variety of soil types. Dye tracing experiments would assist in finding these (Allaire et al., 2009). Sampling soil from the subsoil horizons or non-tilled soil might be interesting to investigate on persistent preferential flow paths since these can be several decades old and enriched with OM (Bundt et al., 2001b, 2000). Furthermore, the flow paths origin (earthworm borrows, roots and cracks) may have an effect on the amount and type of adsorption sites present in the macropore sheaths (Jensen et al., 2002). Pierret et al. (1999) found higher concentrations of Fe and Mn in macropore sheaths and Jensen et al. (2002) found wall materials of cracks to strongly adsorb phosphates. Therefore, beside visualizing the cation adsorption sites another method may be introduced to visualize the anion adsorption sites in undisturbed soils. This could be conducted in a similar way to the here proposed method to visualize cation adsorption sites but with an anion as a contrast agent (e.g. Br^-, WO_4^{2-} or MoO_4^{2-}). This may be meaningful to improve leaching models of phosphate or other anionic pollutants.

The difference image quality could be improved by using the absorption edge technique and a monochromatic X-ray beam. This would eliminate the negative effects of soil movement on the difference image quality, although it would reduce the sample size considerably (Elleaume et al., 2002; Wildenschild et al., 2002).

Conclusions

We have shown that a modern industrial X-ray scanner is capable of providing 3D images that can be used to map the cation adsorption sites in undisturbed soil cores by difference image analyses. Furthermore, Ba^{2+} serves well as a contrast agent to assess the 3D distribution of cation adsorption sites. All undisturbed soil samples showed spatially heterogeneous distributed cation adsorption sites. The highest heterogeneity and highest abundance of cation adsorption sites was observed in an OM rich heavy clay soil from temporally water saturated marshy depression. The silty clay soil from an arable land showed a lower number of cation adsorption sites possible due to lower OM matter contents and desorption of Ba^{2+} from clay surfaces during the rinsing process with KCl. These soils also show less spatial heterogeneity. A loamy sand forest soil with high OM contents showed little spatial heterogeneity. An artificial sample with fine sand and individual clay and OM aggregates showed the highest contrast in cation adsorption between the OM aggregates and the sand and only a small contrast between the clay aggregates and the sand. Our samples showed no clear relation between the abundance of cation adsorption sites and the macropore space. Furthermore, results of the method proposed here to visualize cation adsorption sites in 3D correlates significantly with the results of the ammonium acetate method and the modeled results using Visual MINTEQ. This strengthens the validity of the obtained spatial data on cation adsorption.

References

Allaire, S.E., Roulier, S., Cessna, A.J., 2009. Quantifying preferential flow in soils: A review of different techniques. J. Hydrol. 378, 179–204. doi:10.1016/j.jhydrol.2009.08.013

Altman, S.J., Rivers, M.L., Reno, M.D., Cygan, R.T., McLain, A.A., 2005. Characterization of Adsorption Sites on Aggregate Soil Samples Using Synchrotron X-ray Computerized Microtomography. Environ. Sci. Technol. 39, 2679–2685. doi:10.1021/es049103y

Bodek, I. (Ed.), 1988. Environmental inorganic chemistry: properties, processes, and estimation methods, SETAC special publications series. Pergamon Press, New York.

Bradl, H.B., 2004. Adsorption of heavy metal ions on soils and soils constituents. J. Colloid Interface Sci. 277, 1–18. doi:10.1016/j.jcis.2004.04.005

Bundt, M., Albrecht, A., Froidevaux, P., Blaser, P., Flühler, H., 2000. Impact of Preferential Flow on Radionuclide Distribution in Soil. Environ. Sci. Technol. 34, 3895–3899. doi:10.1021/es9913636

Bundt, M., Jäggi, M., Blaser, P., Siegwolf, R., Hagedorn, F., 2001a. Carbon and Nitrogen Dynamics in Preferential Flow Paths and Matrix of a Forest Soil. Soil Sci. Soc. Am. J. 65, 1529. doi:10.2136/sssaj2001.6551529x

Bundt, M., Widmer, F., Pesaro, M., Zeyer, J., Blaser, P., 2001b. Preferential flow paths: biological “hot spots” in soils. Soil Biol. Biochem. 33, 729–738. doi:10.1016/S0038-0717(00)00218-2

Capowiez, Y., Cadoux, S., Bouchand, P., Roger-Estrade, J., Richard, G., Boizard, H., 2009. Experimental evidence for the role of earthworms in compacted soil regeneration based on field observations and results from a semi-field experiment. Soil Biol. Biochem. 41, 711–717. doi:10.1016/j.soilbio.2009.01.006

Cardoso, E.J.B.N., Vasconcellos, R.L.F., Bini, D., Miyauchi, M.Y.H., Santos, C.A. dos, Alves, P.R.L., Paula, A.M. de, Nakatani, A.S., Pereira, J. de M., Nogueira, M.A., 2013. Soil health: looking for suitable indicators. What should be considered to assess the effects of use and management on soil health? Sci. Agric. 70, 274–289.

Ciesielski, H., Sterckeman, T., 1997. A comparison between three methods for the determination of cation exchange capacity and exchangeable cations in soils. Agronomie 17, 9–16. doi:10.1051/agro:19970102

Darmawan, Wada, S., 1999. Kinetics of speciation of copper, lead, and zinc loaded to soils that differ in cation exchanger composition at low moisture content. Commun. Soil Sci. Plant Anal. 30, 2363–2375. doi:10.1080/00103629909370379

De La Vega, J.C., Häfeli, U.O., 2015. Utilization of nanoparticles as X-ray contrast agents for diagnostic imaging applications. Contrast Media Mol. Imaging 10, 81–95. doi:10.1002/cmmi.1613

Dollinger, J., Dagès, C., Voltz, M., 2015. Glyphosate sorption to soils and sediments predicted by pedotransfer functions. Environ. Chem. Lett. 13, 293–307. doi:10.1007/s10311-015-0515-5

Ekschmitt, K., Kandeler, E., Poll, C., Brune, A., Buscot, F., Friedrich, M., Gleixner, G., Hartmann, A., Kästner, M., Marhan, S., Miltner, A., Scheu, S., Wolters, V., 2008. Soil-carbon preservation through habitat constraints and biological limitations on decomposer activity. J. Plant Nutr. Soil Sci. 171, 27–35. doi:10.1002/jpln.200700051

Elleaume, H., Charvet, A.M., Corde, S., Estève, F., Bas, J.F.L., 2002. Performance of computed tomography for contrast agent concentration measurements with monochromatic x-ray beams: comparison of K-edge versus temporal subtraction. Physics in Medicine and Biology 47.

Ellerbrock, R.H., Gerke, H.H., 2004. Characterizing organic matter of soil aggregate coatings and biopores by Fourier transform infrared spectroscopy. Eur. J. Soil Sci. 55, 219–228.

doi:10.1046/j.1365-2389.2004.00593.x
Essington, M.E., 2004. Organic Matter in Soil, in: Soil and Water Chemistry: An Integrative Approach. CRC Press LLC, pp. 129–180.
FAO, 2014. World reference base for soil resources 2014 international soil classification system for naming soils and creating legends for soil maps. Food and Agriculture Organization of the United Nations, Rome.
FAO, 2006. Guidelines for soil description, 4th ed. ed. Food and Agriculture Organization of the United Nations, Rome.
Figueroa-Diva, R.A., Vasudevan, D., MacKay, A.A., 2010. Trends in soil sorption coefficients within common antimicrobial families. Chemosphere 79, 786–793. doi:10.1016/j.chemosphere.2010.03.017
Gomes, P.C., Fontes, M.P.F., da Silva, A.G., de S. Mendonça, E., Netto, A.R., 2001. Selectivity Sequence and Competitive Adsorption of Heavy Metals by Brazilian Soils. Soil Sci. Soc. Am. J. 65, 1115. doi:10.2136/sssaj2001.6541115x
Guo, L.B., Gifford, R.M., 2002. Soil carbon stocks and land use change: a meta analysis. Glob. Change Biol. 8, 345–360. doi:10.1046/j.1354-1013.2002.00486.x
Gustafsson, J.P., 2012. Visual MINTEQ (v3.1). A Windows version of MINTEQA2.
Gustafsson, J.P., 2001. Modeling the Acid–Base Properties and Metal Complexation of Humic Substances with the Stockholm Humic Model. J. Colloid Interface Sci. 244, 102–112. doi:10.1006/jcis.2001.7871
Hadley Wickham, 2009. ggplot2: Elegant Graphics for Data Analysis. Springer-Verlag, New York.
Horn, R., 1987. Die Bedeutung der Aggregierung für die Nährstoffsorption in Böden. Z. Für Pflanzenernähr. Bodenkd. 150, 13–16. doi:10.1002/jpln.19871500104
Isoyama, M., Wada, S., 2007. Remediation of Pb-contaminated soils by washing with hydrochloric acid and subsequent immobilization with calcite and allophanic soil. J. Hazard. Mater. 143, 636–642. doi:10.1016/j.jhazmat.2007.01.008
Jaremko, D., Kalembasa, D., 2014. A Comparison of Methods for the Determination of Cation Exchange Capacity of Soils/Porównanie Metod Oznaczania Pojemności Wymiany Kationów I Sumy Kationów Wymiennych W Glebach. Ecol. Chem. Eng. S 21. doi:10.2478/eces-2014-0036
Jarvis, N.J., 2007. A review of non-equilibrium water flow and solute transport in soil macropores: principles, controlling factors and consequences for water quality. Eur. J. Soil Sci. 58, 523–546. doi:10.1111/j.1365-2389.2007.00915.x
Jensen, M.B., Hansen, H.C.B., Magid, J., 2002. Phosphate Sorption to Macropore Wall Materials and Bulk Soil. Water, Air and Soil Pollution 137, 141–148. doi:10.1023/A:1015589011729
Johnson, G.., Gupta, K., Putz, D.., Hu, Q., Brusseau, M.., 2003. The effect of local-scale physical heterogeneity and nonlinear, rate-limited sorption/desorption on contaminant transport in porous media. J. Contam. Hydrol. 64, 35–58. doi:10.1016/S0169-7722(02)00103-1
Kabata-Pendias, A., 2010. Trace elements in soils and plants, 4th ed. ed. CRC Press, Boca Raton.
Kahle, M., Kleber, M., Jahn, R., 2003. Retention of dissolved organic matter by illitic soils and clay fractions: Influence of mineral phase properties. J. Plant Nutr. Soil Sci. 166, 737–741. doi:10.1002/jpln.200321125
Kahle, M., Kleber, M., Jahn, R., 2002. Carbon storage in loess derived surface soils from Central Germany: Influence of mineral phase variables. J. Plant Nutr. Soil Sci. 165, 141. doi:10.1002/1522-2624(200204)165:2<141::AID-JPLN141>3.0.CO;2-X
Kim, D., Park, S., Lee, J.H., Jeong, Y.Y., Jon, S., 2007. Antibiofouling Polymer-Coated Gold panoparticles as a Contrast Agent for in Vivo X-ray Computed Tomography Imaging. J. AM. CHEM. SOC. 129, 7661–7665. doi:10.1021/ja071471
Koestel, J., 2016. SoilJ – An ImageJ plugin for semi-automatized image-processing of 3-D X-ray images of soil columns. Geophysical Research Abstracts 18.

Koestel, J., Larsbo, M., 2014. Imaging and quantification of preferential solute transport in soil macropores. Water Resour. Res. 50, 4357–4378. doi:10.1002/2014WR015351
Kögel-Knabner, I., Guggenberger, G., Kleber, M., Kandeler, E., Kalbitz, K., Scheu, S., Eusterhues, K., Leinweber, P., 2008. Organo-mineral associations in temperate soils: Integrating biology, mineralogy, and organic matter chemistry. J. Plant Nutr. Soil Sci. 171, 61–82. doi:10.1002/jpln.200700048
Larsbo, M., Roulier, S., Stenemo, F., Kasteel, R., Jarvis, N., 2005. An Improved Dual-Permeability Model of Water Flow and Solute Transport in the Vadose Zone. Vadose Zone J. 4, 398. doi:10.2136/vzj2004.0137
Lee, S.S., Nagy, K.L., Fenter, P., 2007. Distribution of barium and fulvic acid at the mica–solution interface using in-situ X-ray reflectivity. Geochim. Cosmochim. Acta 71, 5763–5781. doi:10.1016/j.gca.2007.05.031
Leue, M., Ellerbrock, R.H., Gerke, H.H., 2010. DRIFT Mapping of Organic Matter Composition at Intact Soil Aggregate Surfaces. Vadose Zone J. 9, 317. doi:10.2136/vzj2009.0101
Masum, S.A., Kirk, G.J.D., Daly, K.R., Roose, T., 2016. The effect of non-uniform microscale distribution of sorption sites on solute diffusion in soil: Diffusion and microscale heterogeneity. Eur. J. Soil Sci. doi:10.1111/ejss.12353
Murphy, B.W., 2015. Impact of soil organic matter on soil properties—a review with emphasis on Australian soils. Soil Res. 53, 605. doi:10.1071/SR14246
Okada, E., Costa, J.L., Bedmar, F., 2016. Adsorption and mobility of glyphosate in different soils under no-till and conventional tillage. Geoderma 263, 78–85. doi:10.1016/j.geoderma.2015.09.009
Pansu, M., Gautheyrou, J., 2006. Handbook of soil analysis: mineralogical, organic and inorganic methods. Springer, Berlin ; New York.
Pauwels, E., Van Loo, D., Cornillie, P., Brabant, L., Van Hoorebeke, L., 2013. An exploratory study of contrast agents for soft tissue visualization by means of high resolution X-ray computed tomography imaging. J. Microsc. 250, 21–31. doi:10.1111/jmi.12013
Peth, S., Chenu, C., Leblond, N., Mordhorst, A., Garnier, P., Nunan, N., Pot, V., Ogurreck, M., Beckmann, F., 2014. Localization of soil organic matter in soil aggregates using synchrotron-based X-ray microtomography. Soil Biol. Biochem. 78, 189–194. doi:10.1016/j.soilbio.2014.07.024
Pichtel, J., Kuroiwa, K., Sawyerr, H.., 2000. Distribution of Pb, Cd and Ba in soils and plants of two contaminated sites. Environ. Pollut. 110, 171–178. doi:10.1016/S0269-7491(99)00272-9
Pierret, A., Moran, C., Pankhurst, C., 1999. Differentiation of soil properties related to the spatial association of wheat roots and soil macropores. Plant and Soil 211, 51–58.
Porfiri, C., Montoya, J.C., Koskinen, W.C., Azcarate, M.P., 2015. Adsorption and transport of imazapyr through intact soil columns taken from two soils under two tillage systems. Geoderma 251–252, 1–9. doi:10.1016/j.geoderma.2015.03.016
Preibisch, S., Saalfeld, S., Schindelin, J., Tomancak, P., 2010. Software for bead-based registration of selective plane illumination microscopy data. Nat. Methods 7, 418–419. doi:10.1038/nmeth0610-418
R Core Team, 2016. A Language and Environment for Statistical Computing. R Foundation for Statistical Computing, Vienna, Austria.
Ruamps, L.S., Nunan, N., Chenu, C., 2011. Microbial biogeography at the soil pore scale. Soil Biol. Biochem. 43, 280–286. doi:10.1016/j.soilbio.2010.10.010
Schindelin, J., Arganda-Carreras, I., Frise, E., Kaynig, V., Longair, M., Pietzsch, T., Preibisch, S., Rueden, C., Saalfeld, S., Schmid, B., Tinevez, J.-Y., White, D.J., Hartenstein, V., Eliceiri, K., Tomancak, P., Cardona, A., 2012. Fiji: an open-source platform for biological-image analysis. Nat. Methods 9, 676–682. doi:10.1038/nmeth.2019
Schindelin, J., Rueden, C.T., Hiner, M.C., Eliceiri, K.W., 2015. The ImageJ ecosystem: An open

platform for biomedical image analysis. Mol. Reprod. Dev. 82, 518–529. doi:10.1002/mrd.22489
Teferi, E., Bewket, W., Simane, B., 2016. Effects of land use and land cover on selected soil quality indicators in the headwater area of the Blue Nile basin of Ethiopia. Environ. Monit. Assess. 188. doi:10.1007/s10661-015-5086-1
Thieme, J., Schneider, G., Knöchel, C., 2003. X-ray tomography of a microhabitat of bacteria and other soil colloids with sub-100 nm resolution. Micron 34, 339–344. doi:10.1016/S0968-4328(03)00061-1
Tracy, S.R., Roberts, J.A., Black, C.R., McNeill, A., Davidson, R., Mooney, S.J., 2010. The X-factor: visualizing undisturbed root architecture in soils using X-ray computed tomography. J. Exp. Bot. 61, 311–313. doi:10.1093/jxb/erp386
Van Loo, D., Bouckaert, L., Leroux, O., Pauwels, E., Dierick, M., Van Hoorebeke, L., Cnudde, V., De Neve, S., Sleutel, S., 2014. Contrast agents for soil investigation with X-ray computed tomography. Geoderma 213, 485–491. doi:10.1016/j.geoderma.2013.08.036
Wildenschild, D., Vaz, C.M.., Rivers, M.L., Rikard, D., Christensen, B.S.B., 2002. Using X-ray computed tomography in hydrology: systems, resolutions, and limitations. J. Hydrol. 267, 285–297. doi:10.1016/S0022-1694(02)00157-9
Young, I.M., Crawford, J.W., Nunan, N., Otten, W., Spiers, A., 2008. Chapter 4 Microbial Distribution in Soils, in: Advances in Agronomy. Elsevier, pp. 81–121.